

Balanced Diffusion-Guided Fusion for Multimodal Remote Sensing Classification

Hao Liu, Yongjie Zheng, Yuhan Kang, Mingyang Zhang, *Member, IEEE*,

Maoguo Gong, *Fellow, IEEE*, Lorenzo Bruzzone, *Fellow, IEEE*

Abstract—Deep learning-based techniques for the analysis of multimodal remote sensing data have become popular due to their ability to effectively integrate spatial, spectral, and structural information from different sensors. Recently, denoising diffusion probabilistic models (DDPMs) have attracted attention in the remote sensing community due to their powerful ability to capture robust and complex spatial-spectral distributions. However, pre-training multimodal DDPMs may result in modality imbalance, and effectively leveraging diffusion features to guide complementary diversity feature extraction remains an open question. To address these issues, this paper proposes a balanced diffusion-guided fusion framework that leverages multimodal diffusion features to guide a multi-branch network for land-cover classification. Specifically, we propose an adaptive modality masking strategy to encourage the DDPMs to obtain a modality-balanced rather than spectral image-dominated data distribution. Subsequently, these diffusion features hierarchically guide feature extraction among CNN, Mamba, and transformer networks by integrating feature fusion, group channel attention, and cross-attention mechanisms. Finally, a mutual learning strategy is developed to enhance inter-branch collaboration by aligning the probability entropy and feature similarity of individual subnetworks. Extensive experiments on four multimodal remote sensing datasets demonstrate that the proposed method achieves superior classification performance. The code is available at <https://github.com/HaoLiu-XDU/BDGF>.

Index Terms—Multimodal, diffusion models, feature fusion, image classification, hyperspectral and multispectral images, synthetic aperture radar, remote sensing.

I. INTRODUCTION

MULTIMODAL remote sensing data typically comprises images from various sensors, including hyperspectral images (HSI), synthetic aperture radar (SAR), and light detection and ranging. By fusing complementary spatial, spectral, and structural information, multimodal data facilitates an accurate classification [1], thereby supporting applications in environmental monitoring [2], [3], urban planning [4], and resource exploration [5].

Hao Liu, Yongjie Zheng, and Lorenzo Bruzzone are with the Department of Information Engineering and Computer Science, University of Trento, 38123 Trento, Italy (e-mail: hao.liu@unitn.it; yongjie.zheng@unitn.it; lorenzo.bruzzone@unitn.it). (*Corresponding author: Lorenzo Bruzzone*).

Yuhan Kang is with the College of Electrical and Information Engineering, Hunan University, Changsha 410082, China (e-mail: kyh433@hnu.edu.cn).

Mingyang Zhang is with the Key Laboratory of Collaborative Intelligent Systems of Ministry of Education, Xidian University, Xi'an 710071, China (e-mail: omegazhangmy@gmail.com).

Maoguo Gong is with the Key Laboratory of Collaborative Intelligence Systems, Ministry of Education, Xidian University, Xi'an 710071, and the Academy of Artificial Intelligence, Inner Mongolia Normal University, Hohhot 010028, China (email:gong@ieee.org).

In recent years, deep learning methods have revolutionized multimodal remote sensing image classification. Regarding feature extraction and fusion strategy, network architectures are primarily based on convolutional neural networks (CNNs), Transformers, and Mamba models.

CNNs serve as the foundation of many multimodal frameworks due to their ability to capture local spatial patterns through convolutional filters and feature learning [6], [7]. For instance, Hong et al. [8] proposed a CNN-based framework with various fusion strategies, and Wu et al. [9] combined CNNs with a cross-channel reconstruction module. These methods typically use separate CNNs to extract features from each modality and concatenate them along the channel dimension to further learn joint representations. However, CNNs are inherently limited by their receptive fields, which can constrain the modeling of long-range dependencies essential for understanding complex remote sensing scenes.

Transformers mitigate this shortcoming through self-attention mechanisms that capture global context [10]. Xue et al. [11] introduced a deep hierarchical vision transformer leveraging self-attention for spatial features and spectral sequences. Roy et al. [12] proposed a multimodal fusion transformer with a multihead cross-patch attention framework. In addition, numerous transformer-based studies have proposed different fusion strategies [13], [14], multiscale feature transformers [15], and global-local structures [16]. Moreover, the Mamba model [17] has gained popularity for capturing long-range dependencies with improved computational efficiency. Building on the Mamba architecture, researchers have developed diffusion-based Mamba [18], spatial-spectral Mamba [19], and multi-scale Mamba [20], [21] variants. In terms of multimodal fusion strategies, Transformer-based methods typically employ global cross-attention mechanisms at the token level, while Mamba-based approaches optimize Mamba blocks to simultaneously perform multimodal fusion and model long-range dependencies. Adaptively merging these local, long-range, and sequence-aware representations can leverage their strengths and compensate for their weaknesses [22]–[24].

However, most existing methods are primarily designed to extract features for downstream classification task, which limits their ability to capture the complex, high-dimensional, and redundant distributions characteristic of remote sensing data. In addition, challenges remain in modeling complementary diversity features [25], [26] and ensuring robustness to noisy remote sensing data [27].

Diffusion-based two-stage methods have emerged as a promising alternative to other deep learning models for remote

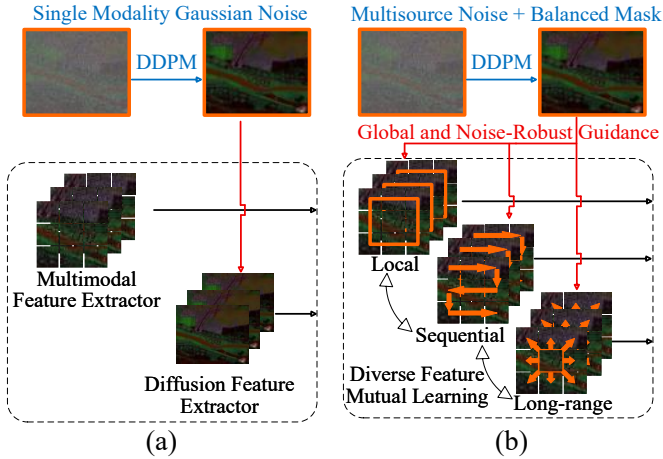


Fig. 1. Comparison of workflows. (a) Previous methods process diffusion and multimodal features separately and then combine them for joint classification. (b) In this work, we exploit global and noise-robust diffusion information to guide the mutual learning of local, sequence-level, and long-range features.

sensing image interpretation [28]. By iteratively refining noisy inputs, denoising diffusion probabilistic models (DDPMs) learn robust and noise-reduced representations that capture complex data distributions [29], [30]. For example, Chen et al. [31] and Chen et al. [32] both employed a diffusion model to extract high-dimensional and redundant distribution from HSI. In [33] and [34], the multi-step iterative denoising process was used for fusing multi-time-step features for HSI classification. In multimodal scenarios, Zhang et al. [35] only integrated HSI diffusion features instead of multimodal information into the downstream network, which is essentially hyperspectral feature extraction and classification. Typically, these methods rely on a two-stage pre-training paradigm to train the denoising and feature interpretation networks. To reduce the high computational complexity of heavy pre-training models, it is possible to merge multimodal images into a single pre-training network [36]. However, studies [37]–[39] have observed that the modality with more discriminative information tends to dominate the optimization process, leading to the problem of modality imbalance.

Although recent advancements have yielded significant improvements, limitations still remain:

- 1) Concatenating the image’s channel dimension into a single network can reduce the computational complexity of the pre-trained model [36]. However, this approach introduces a severe modality imbalance problem, as spectral images typically contain more data than SAR images, causing HSIs to dominate the optimization process.
- 2) DDPMs capture complex remote sensing distributions for previous task-oriented models. However, few studies have employed global and noise-robust diffusion information to guide the extraction of various characteristics, including local, long-range, and sequence-aware features.
- 3) While prior research has emphasized fusing complementary features across various stages of the network, there are limited auxiliary learning cues, such as posterior uncertainty and feature similarity, to enhance knowledge sharing among branches.

Fig. 1 compares the workflows and illustrates the motivation behind our approach. To address these challenges, this paper introduces a balanced diffusion-guided fusion (BDGF) method that employs a pre-training DDPM to guide a multi-branch network for multimodal land-cover classification. Initially, an adaptive modality masking strategy is proposed to pre-train the diffusion model and obtain modality-balanced multimodal diffusion features. Subsequently, these diffusion features guide the CNNs, Mamba, and transformer networks of the multi-branch network through feature fusion, group channel attention, and cross-attention fusion. Finally, a mutual learning approach dynamically enhances collaboration among the branches and achieves classification based on the probability entropy and feature similarity of each sub-network. The main contributions of this paper are as follows:

- 1) We propose an adaptive modality masking strategy for DDPMs that encourages the model to focus on all information source images by progressively masking dominant images, thereby obtaining diffusion features that reflect the complex intrinsic distribution of multimodal data.
- 2) We introduce a diffusion-guided fusion strategy that leverages multimodal diffusion information to hierarchically guide the fusion of diverse features based on the global characteristics of different branches.
- 3) We present a multi-branch network mutual learning strategy that dynamically promotes feature complementarity among networks through predicted probability entropy and pairwise similarity.
- 4) Experiments on four multimodal RS datasets show our method outperforms state-of-the-art under diverse sample numbers.

The remainder of this paper is organized as follows. Section II provides background on the BDGF methodology. Section III describes the proposed method in detail. Section IV validates the method on four real remote sensing datasets. Finally, Section V draws the conclusions of this paper.

II. RELATED WORK

This section first reviews the background and advanced methods based on diffusion models in remote sensing, followed by a discussion of techniques for multimodal remote sensing feature fusion.

A. Denoising Diffusion Probabilistic Model

The DDPM [29] is a widely adopted deep generative model [30]. Pre-training a DDPM involves both a forward diffusion process and a reverse diffusion process. Given an image \mathbf{x}_0 , the noisy image \mathbf{x}_t at time t can be obtained through a Markov chain:

$$\begin{cases} \mathbf{x}_t = \sqrt{\bar{\alpha}_t} \mathbf{x}_0 + \sqrt{1 - \bar{\alpha}_t} \epsilon, \\ \bar{\alpha}_t = \prod_{i=1}^t \alpha_i, \end{cases} \quad (1)$$

where ϵ represents the noise and α_t denotes the noise scaling factor. The transfer probability $q(\mathbf{x}_t | \mathbf{x}_{t-1})$ is defined as:

$$q(\mathbf{x}_t | \mathbf{x}_{t-1}) = \mathcal{N}(\mathbf{x}_t; \sqrt{\alpha_t} \mathbf{x}_{t-1}, (1 - \alpha_t) \mathbf{I}), \quad (2)$$

where \mathbf{I} is the identity matrix. Here, $\mu_t = \sqrt{\alpha_t}\mathbf{x}_{t-1}$ and $\sigma_t^2 = (1 - \alpha_t)\mathbf{I}$ are the mean value and the variance, respectively.

In the reverse process, the model predicts the clean data \mathbf{x}_{t-1} given \mathbf{x}_t . The conditional probability is expressed as:

$$p_\theta(\mathbf{x}_{t-1}|\mathbf{x}_t) = \mathcal{N}(\mathbf{x}_{t-1}; \mu_\theta(\mathbf{x}_t, t), \sigma_\theta^2(\mathbf{x}_t, t)), \quad (3)$$

where μ_θ and σ_θ^2 are the predicted mean and variance, parameterized by the model. The predicted mean $\mu_\theta(\mathbf{x}_t, t)$ is typically defined as:

$$\mu_\theta(\mathbf{x}_t, t) = \frac{1}{\sqrt{\alpha_t}} \left(\mathbf{x}_t - \frac{1 - \alpha_t}{\sqrt{1 - \alpha_t}} \epsilon_\theta(\mathbf{x}_t, t) \right), \quad (4)$$

where $\epsilon_\theta(\mathbf{x}_t, t)$ represents the noise predicted by the model.

DDPMs can recover the target distribution through iterative denoising, thereby effectively promoting remote sensing image interpretation tasks [28]. Many studies utilize DDPMs to capture the data distribution of complex images and integrate the extracted features at one [32] or multiple time steps [34] into various tasks during training, such as classification [31], [33], change detection [40], [41], image matching [42], and object detection [43]. In the content of multimodal data analysis, Zhang et al. [35] fused the HSI image features extracted by DDPMs into a downstream multi-branch network. Du et al. [18] integrated diffusion feature into mamba structure for semantic segmentation.

However, these methods rarely leverage the global guidance provided by diffusion features. Meanwhile, solely extracting diffusion features from HSIs does not satisfy the requirements for multimodal classification. To address these issues, this paper proposes an improved DDPM to obtain modality-balanced multimodal diffusion features. In addition, a series of feature extraction and classification techniques are designed to guide the downstream multi-branch network.

B. Multimodal Multi-Branch Network

The heterogeneity of multimodal remote sensing data prevents a single model from effectively capturing both local features and global dependencies [22], [44]. To address this limitation, numerous hybrid algorithms have been developed to leverage the strengths of different architectures, such as CNNs' local inductive bias [8], [9], transformers' global attention mechanisms [12], and Mamba's efficient long-sequence modeling [20]. In addition, multi-branch architectures enable independent encoding and interactive fusion of heterogeneous modalities, significantly enhancing the model's ability to capture cross-modal semantic associations.

Several studies have explored the above-mentioned architectures. Gao et al. [10] combined CNNs for local feature extraction with transformers for global feature modeling. Xue et al. [11] embedded convolutional operations into spatial and spectral hierarchical transformers to capture both global and local features. Tu et al. [16] proposed a fusion strategy based on multi-scale information and a dual-branch structure to integrate global and local representations. Zhang et al. [19] introduced Cross-SSM, which extracts multimodal state information by integrating CNNs and Mamba. Liao et al. [25] mitigated feature diversity challenges by developing a

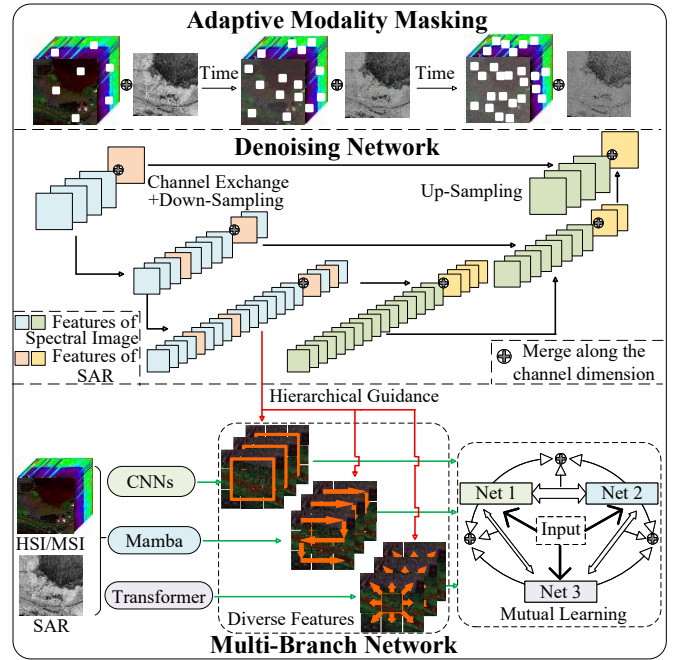


Fig. 2. Illustration of the proposed BDGF framework.

multimodal classification network incorporating multiple architectural structures.

These methods extract diverse global and local features through hybrid or parallel structures, improving feature extraction and classification. In this paper, we propose integrating robust and complex diffusion features as guiding knowledge into a multi-branch network and further enhance the collaboration of diverse features through mutual learning.

III. METHODOLOGY

The proposed BDGF is designed to use diffusion distribution to guide the complementarity of diverse features. Fig. 2 illustrates the overall BDGF framework. In the pre-training phase, the denoising network generates modality-balanced diffusion features using an adaptive modality masking strategy. During training, these features hierarchically guide the extraction and fusion of information within the multi-branch network. Finally, the mutual learning module enhances the alignment of multimodal features. The following subsections provide a detailed explanation of each module within the BDGF framework.

A. Adaptive Modality Masking-Based DDPMs

DDPMs excel at extracting noise-reduced and robust representations that capture complex data distributions, which are beneficial for feature extraction and classification. To fully exploit the advantages of DDPMs in multimodal remote sensing images, we improve the model with respect to remote sensing image noise, multimodal fusion, and modality imbalance. The overall structure is shown in Fig. 3.

Let us focus the attention on the most typical information source in remote sensing, i.e. SAR and spectral images. SAR images are severely disturbed by speckle noise [45], which

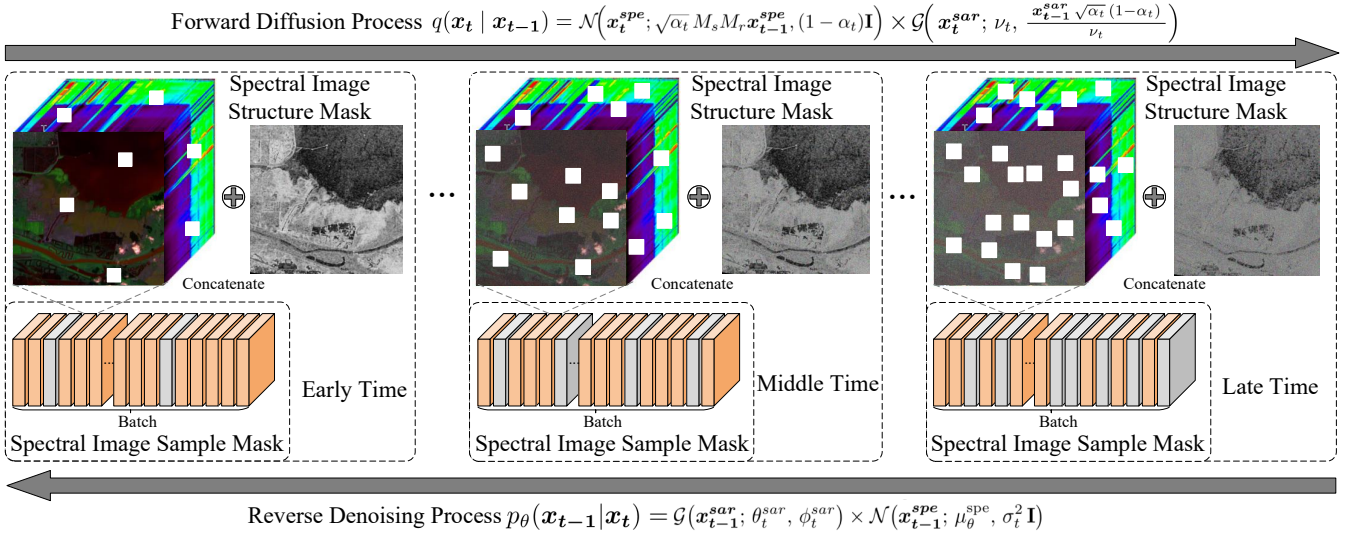


Fig. 3. Structure of the adaptive modality masking strategy. In the forward diffusion process, the strategy consists of adding an iteration-varying structure mask and sample mask to the spectral image, while adding noise to the multimodal data.

makes it difficult to extract discriminative features. For an L -look SAR image, speckle noise is typically modeled as multiplicative noise n . With mean I and variance $1/L$, the gamma-distributed probability density function is defined as:

$$p_{sar}(n) = \left(\frac{L}{I}\right)^L \frac{n^{L-1}}{\Gamma(L)} \exp\left(-\frac{Ln}{I}\right), \quad (5)$$

where $\Gamma(\cdot)$ denotes the gamma function. In contrast, noise in spectral images is typically modeled as an additive process following a Gaussian distribution. In this context, the additive noise n is assumed to have zero mean and variance σ^2 , with the probability density function given by:

$$p_{spe}(n) = \frac{1}{\sqrt{2\pi\sigma^2}} \exp\left(-\frac{n^2}{2\sigma^2}\right). \quad (6)$$

An advantage of merging SAR and spectral images is the reduction in computational complexity during pre-training [36]. However, spectral images, which contain more discriminative information, tend to dominate the optimization process, causing DDPMs to gradually overlook the complementary information provided by SAR images.

Inspired by [37], [39], we aim to prevent DDPMs from over-focusing on spectral images. Unlike reconstruction tasks that add large blocks of masks from a spatial or spectral perspective [46], [47], our strategy dynamically employs a sample mask m_s and a structure mask m_r for spectral images \mathbf{x}_m^{spe} . The sample mask m_s reduces the proportion of the dominant modality in the batch, while m_r randomly masks a certain proportion of the image using a minimal $1 \times 1 \times 1$ block. To dynamically suppress the dominant modality, the mask ratio is continuously increased during the iterative process. Assuming that $epoch \in [0, 1]$ represents the training progress, the mask generation can be expressed as:

$$m \sim \text{Bernoulli}\left(\frac{\exp(epoch) - \exp(-epoch)}{\exp(epoch) + \exp(-epoch)}\right), \quad (7)$$

where *Bernoulli* is Bernoulli distribution and \exp is an ex-

ponential operation. This soft distribution allows unbiased and element-wise random masking based on the iteration progress. Based on (5)-(7), we add multiplicative speckle noise to the SAR image \mathbf{x}_0^{sar} and Gaussian noise to the spectral image \mathbf{x}_0^{spe} . Then, we merge them along the channel dimension. (1) can be transformed into:

$$\begin{cases} \mathbf{x}_t = \sqrt{\alpha_t} \begin{bmatrix} \prod_{i=1}^t n_i^s \odot \mathbf{x}_0^{sar} \\ M_s M_r \mathbf{x}_0^{spe} \end{bmatrix} + \sqrt{1 - \alpha_t} \begin{bmatrix} 0 \\ \epsilon_p \end{bmatrix}, \\ \bar{\alpha}_t = \prod_{i=1}^t n_i \alpha_i, M = \text{diag}(m), n_i^s \sim p_{sar}, \epsilon_p \sim p_{spe}. \end{cases} \quad (8)$$

Given ν_t and \mathcal{G} as SAR Gamma shape and distribution respectively, the transfer probability of forward diffusion process (2) can be expressed as:

$$\begin{cases} q(\mathbf{x}_t | \mathbf{x}_{t-1}) = q^{sar}(\mathbf{x}_t^{sar} | \mathbf{x}_{t-1}^{sar}) \times q^{spe}(\mathbf{x}_t^{spe} | \mathbf{x}_{t-1}^{spe}), \\ q^{spe}(\mathbf{x}_t^{spe} | \mathbf{x}_{t-1}^{spe}) = \mathcal{N}(\mathbf{x}_t^{spe}; \sqrt{\alpha_t} M_s M_r \mathbf{x}_{t-1}^{spe}, (1 - \alpha_t) \mathbf{I}), \\ q^{sar}(\mathbf{x}_t^{sar} | \mathbf{x}_{t-1}^{sar}) = \mathcal{G}(\mathbf{x}_t^{sar}; \nu_t, \frac{\mathbf{x}_{t-1}^{sar} \sqrt{\alpha_t} (1 - \alpha_t)}{\nu_t}). \end{cases} \quad (9)$$

Correspondingly, the transfer probability of reverse diffusion process (3) can be expressed as:

$$p_\theta(\mathbf{x}_{t-1} | \mathbf{x}_t) = \mathcal{G}(\mathbf{x}_{t-1}^{sar}; \theta_t^{sar}, \phi_t^{sar}) \times \mathcal{N}(\mathbf{x}_{t-1}^{spe}; \mu_\theta^{spe}, \sigma_t^2 \mathbf{I}), \quad (10)$$

where θ_t^{sar} and ϕ_t^{sar} are the Gamma shape and scale, respectively. μ_θ^{spe} and σ_t^2 are mean and variance similar to (3). The denoising network updates its parameters via gradient descent. The pseudo-code is shown in Algorithm 1.

Fig. 4 visualizes the distribution effect of the features obtained by the proposed method on the LCZ HK dataset. The t-SNE execution details are the same as in Section IV-C. Across categories the adaptive multimodality masking (a) produces more uniform, consolidated class clusters and reduces dominance and fragmentation seen in the original model. For example, class C6 forms a tight, isolated cluster in (a) but is scattered and intermixed with other classes in (b).

Algorithm 1 Adaptive Modality Masking Strategy

Require: Original data $\mathbf{x}_0^{sar}, \mathbf{x}_0^{spe}$; current training progress $epoch \in [0, 1]$; diffusion schedule $\bar{\alpha}_t$.

1. Dynamic Mask Generation:

Compute mask probability: $p \leftarrow \frac{\exp(epoch) - \exp(-epoch)}{\exp(epoch) + \exp(-epoch)}$

Compute sample and structure masks: m_s, m_r

Construct diagonal mask matrices: $M_s = \text{diag}(m_s), M_r = \text{diag}(m_r)$

2. Noisy Multimodal Data Generation:

Sample time step t

Sample multiplicative speckle noise: $n^s \sim p_{sar}$

Sample Gaussian noise: $\epsilon_p \sim \mathcal{N}(0, \mathbf{I})$

Construct multimodal noisy state \mathbf{x}_t :

$$\mathbf{x}_t \leftarrow \left[\begin{array}{c} \sqrt{\bar{\alpha}_t} (\prod_{i=1}^t n_i^s \odot \mathbf{x}_0^{sar}) \\ \sqrt{\bar{\alpha}_t} (M_s M_r \mathbf{x}_0^{spe}) + \sqrt{1 - \bar{\alpha}_t} \epsilon_p \end{array} \right]$$

3. Diffusion Process and Noise Prediction:

Generate forward diffusion:

$$q(\mathbf{x}_t | \mathbf{x}_{t-1}) = q^{sar}(\mathbf{x}_t^{sar} | \mathbf{x}_{t-1}^{sar}) \times q^{spe}(\mathbf{x}_t^{spe} | \mathbf{x}_{t-1}^{spe})$$

Generate reverse denoising:

$$p_\theta(\mathbf{x}_{t-1} | \mathbf{x}_t) = \mathcal{G}(\mathbf{x}_{t-1}^{sar}; \theta_t^{sar}, \phi_t^{sar}) \times \mathcal{N}(\mathbf{x}_{t-1}^{spe}; \mu_\theta^{spe}, \sigma_\theta^2 \mathbf{I})$$

Predict noise and update parameters.

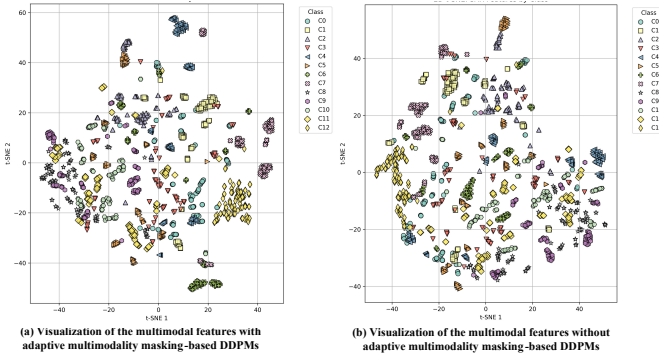


Fig. 4. 2D t-SNE embeddings of diffusion feature distribution on the LCZ HK dataset.

B. Diffusion Features Guidance

To leverage the multimodal data distribution extracted through the diffusion process, the diffusion features guide the extraction of diverse features in accordance with the characteristics of each branch. CNN-based architectures capture local features using small convolution kernels, whereas transformers and Mamba models extract global features via attention mechanisms and state space models. Mamba is particularly well-suited for tasks involving long sequence features [48]. Section IV-C presents a detailed visualization analysis of the complementarity of multi-branch network features.

1) *CNN-Based Network:* CNN networks extract local information that differs significantly from diffusion features. Therefore, as shown in Fig. 5, the diffusion data distribution is deeply integrated into feature generation via a feature fusion approach. Given the spectral image \mathbf{x}^{spec} , SAR image \mathbf{x}^{sar} , and diffusion features \mathbf{f}^{dif} as inputs, the process is expressed as follows:

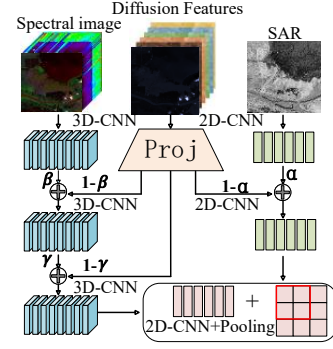


Fig. 5. Flowchart of diffusion features guide CNN-based network.

$$\begin{aligned} \mathbf{f}_{cnn}^1 &= \beta \cdot w_1^{3d} \mathbf{x}^{spec} + (1 - \beta) \cdot w_1^{2d} \mathbf{f}^{dif}, \\ \mathbf{f}_{cnn}^2 &= \gamma \cdot w_2^{3d} \mathbf{f}_{cnn}^1 + (1 - \gamma) \cdot w_2^{2d} \mathbf{f}^{dif}, \\ \mathbf{f}_{cnn}^3 &= \alpha \cdot w_4^{2d} \mathbf{x}^{sar} + (1 - \alpha) \cdot w_3^{2d} \mathbf{f}^{dif}, \end{aligned} \quad (11)$$

where w^{3d} and w^{2d} denote three-dimensional and two-dimensional convolution operations, respectively. The intermediate feature vectors \mathbf{f}_{cnn}^1 , \mathbf{f}_{cnn}^2 , and \mathbf{f}_{cnn}^3 are produced during the network's processing, and α , β , and γ are trainable scalar parameters. The output of the feature fusion-based CNN module is given by:

$$\mathbf{f}_{cnn} = w_6^{2d} (w_3^{3d} \mathbf{f}_{cnn}^2 + w_5^{2d} \mathbf{f}_{cnn}^3). \quad (12)$$

2) *Transformer-Based Network:* The transformer exploits attention mechanisms to extract global information, a key aspect of feature diversity. As shown in Fig. 6, the transformer-based network comprises trainable mapping tensors for preliminary processing of multimodal data and a cross-attention fusion module to facilitate global feature interaction. Given the spectral image \mathbf{x}^{spec} , the output $\mathbf{f}_{trans}^{spec}$ of spatial attention and trainable mapping is computed as:

$$\mathbf{f}_{trans}^{spec} = \text{Soft} \cdot (\mathbf{W}_1^{att} \cdot w_7^{2d} \mathbf{x}^{spec}) \cdot \mathbf{W}_1^{map} \cdot \mathbf{x}^{spec}, \quad (13)$$

where \mathbf{W}_1^{att} and Soft denote a trainable tensor and an activation function, respectively, to obtain the spatial importance. The tensor \mathbf{W}_1^{map} maps features to a common dimension, and w_7^{2d} represents a two-dimensional convolution operation. Similarly, the intermediate feature \mathbf{f}_{trans}^{sar} is obtained from the SAR image \mathbf{x}^{sar} . The diffusion features, after tensor mapping, are given by:

$$\mathbf{f}_{trans}^{dif} = \mathbf{W}_2^{map} \cdot \mathbf{f}^{dif}, \quad (14)$$

where \mathbf{W}_2^{map} is a mapping tensor for processing diffusion features.

Furthermore, inspired by [49], [50], cross-attention fusion is employed to share abstract classification information among spectral, SAR, and diffusion features. Taking spectral features as an example, the \mathbf{Q} , \mathbf{K} , and \mathbf{V} in the self-attention mechanism are computed as:

$$\mathbf{Q}, \mathbf{K}, \mathbf{V} = FC \cdot \mathbf{f}_{trans}^{spec}, \quad (15)$$

where FC represents linear layers that generate attention vectors with the same dimensionality as the input. The self-

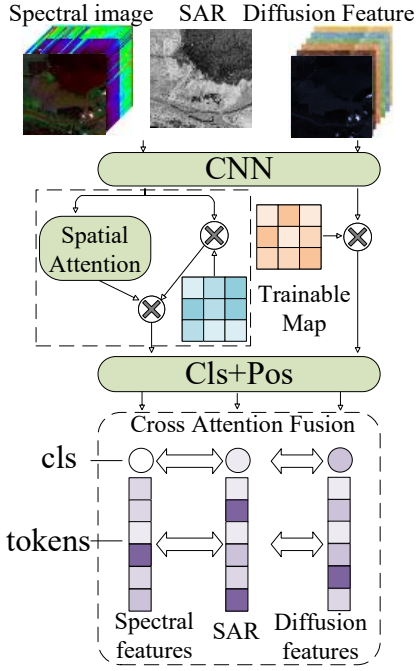


Fig. 6. Illustration of transformer-based network structure.

attention mechanism then produces a new feature vector:

$$\mathbf{F}^{spec} = \mathbf{V} \cdot \text{Soft} \left(\frac{\mathbf{Q} \cdot \mathbf{K}^T}{\sqrt{d_k}} \right) + \mathbf{f}_{trans}^{spec}, \quad (16)$$

where d_k denotes the dimension of \mathbf{K} . Similarly, self-attention is applied to obtain \mathbf{F}^{sar} and \mathbf{F}^{dif} for the SAR and diffusion features, respectively. These vectors comprise both class tokens and patch tokens. Spectral and SAR images can be expressed as $\mathbf{F}^{spec} = \mathbf{F}_{cls}^{spec} \cup \mathbf{F}_{tok}^{spec}$ and $\mathbf{F}^{sar} = \mathbf{F}_{cls}^{sar} \cup \mathbf{F}_{tok}^{sar}$.

Subsequently, the cross attention vectors are computed as:

$$\mathbf{Q}^{spec} = \mathbf{W}_Q \mathbf{F}_{cls}^{spec}, \quad \mathbf{K}^{sar} = \mathbf{W}_K \mathbf{F}_{tok}^{sar}, \quad \mathbf{V}^{sar} = \mathbf{W}_V \mathbf{F}_{tok}^{sar}, \quad (17)$$

where \mathbf{W}_Q , \mathbf{W}_K , and \mathbf{W}_V are trainable weight tensors. The new spectral feature is then computed as:

$$\mathbf{F}_{trans}^{spec} = \left(\mathbf{V}^{sar} \cdot \text{Soft} \frac{\mathbf{Q}^{spec} \cdot (\mathbf{K}^{sar})^T}{\sqrt{d_k^{sar}}} + \mathbf{F}_{trans}^{spec} \right) \cup \mathbf{F}_{tok}^{spec}, \quad (18)$$

where d_k^{sar} represents the dimension of \mathbf{K}^{sar} . Similarly, \mathbf{F}_{trans}^{sar} is computed. Finally, after combining $\mathbf{F}_{trans}^{spec}$ and \mathbf{F}_{trans}^{sar} , the merged feature is processed with \mathbf{F}^{dif} in a manner analogous to (17) and (18) to obtain $\mathbf{F}_{trans}^{diff}$. The final output of the transformer-based network is:

$$\mathbf{f}_{trans} = \mathbf{F}_{trans}^{spectral} + \mathbf{F}_{trans}^{sar} + \mathbf{F}_{trans}^{diff}. \quad (19)$$

3) *Mamba-Based Network*: Fig. 7 illustrates the flowchart of the Mamba-based network, which incorporates Mamba blocks to extract long-sequence information and a group attention module to alleviate data imbalance.

Spectral images naturally yield longer sequences compared to SAR images. However, spectral redundancy can cause a modality imbalance that restricts the information extraction capability of Mamba. To address this limitation, we integrate

local CNN features from (12) and global diffusion features, employing a balanced global-local group attention mechanism to handle redundant spectral dimensions.

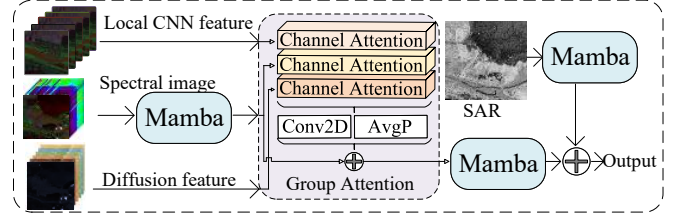


Fig. 7. Flowchart of the proposed Mamba-based network.

Taking the spectral image \mathbf{x}^{spec} as input, the operations in Mamba are defined as:

$$\begin{aligned} \mathbf{F}_m^{spec} &= (\text{SSM} \cdot \text{FC} \cdot \mathbf{x}^{spec}) \otimes (\text{FC} \cdot \mathbf{x}^{spec}), \\ \mathbf{f}_m^{spec} &= (\text{FC} \cdot \mathbf{F}_m^{spec}) \oplus \mathbf{x}^{spec}, \end{aligned} \quad (20)$$

where \mathbf{F}_m^{spec} is the intermediate feature produced by the Mamba blocks, \mathbf{f}_m^{spec} is the final output, SSM denotes the SSM module with the selective scan mechanism, and \otimes , \oplus denote appropriate fusion operations. Similarly, the SAR image \mathbf{x}^{sar} yields features \mathbf{f}_m^{sar} .

Subsequently, \mathbf{f}_m^{spec} , \mathbf{f}_m^{dif} , and \mathbf{f}_{cnn} from (12) are used to construct group attention. Assuming the input feature is \mathbf{f} , the attention mechanism is expressed as:

$$\begin{aligned} \mathbf{Q}_m, \mathbf{K}_m, \mathbf{V}_m &= w_8^{2d}(\mathbf{f}), w_9^{2d}(\mathbf{f}), w_{10}^{2d}(\mathbf{f}), \\ \mathbf{E}_m &= \mathbf{Q}_m \cdot \mathbf{K}_m^T, \end{aligned} \quad (21)$$

where \mathbf{Q}_m , \mathbf{K}_m , \mathbf{V}_m and \mathbf{E}_m are the vectors in the attention mechanism. w_8^{2d} , w_9^{2d} , and w_{10}^{2d} denote two-dimensional convolution operations. For each i and j dimension of tensor \mathbf{E}_m , we update it to obtain the attention score \mathbf{A}_m by taking the maximum along the j dimension and expanding its shape:

$$\begin{aligned} \mathbf{E}'_{i,j} &= \max_j \mathbf{E}_{i,j} - \mathbf{E}_{i,j}, \\ \mathbf{A}_m &= \mathbf{V}_m \cdot \text{Soft}(\mathbf{E}'_m), \end{aligned} \quad (22)$$

where \mathbf{E}'_m denotes the updated tensor from (21). The output of the single-channel attention is:

$$\mathbf{f}_{CA} = \lambda \mathbf{A}_m + \mathbf{V}_m, \quad (23)$$

where λ as a trainable scaling parameter. Similarly, we obtain outputs \mathbf{f}_{CA}^{spec} , \mathbf{f}_{CA}^{dif} , and \mathbf{f}_{CA}^{cnn} . The output of the group attention module is given by:

$$\mathbf{F}_{GA}^{spec} = w_{11}^{2d} \left(\mathbf{f}_{CA}^{spec}, \mathbf{f}_{CA}^{dif}, \mathbf{f}_{CA}^{cnn} \right) \cdot \mathbf{f}_m^{spec} + \mathbf{f}_m^{spec}. \quad (24)$$

Finally, based on \mathbf{f}_m^{sar} in (20) and \mathbf{F}_{GA}^{spec} in (24), the output of the Mamba-based network \mathbf{f}_{mamba} is obtained.

C. Mutual Learning Module

The mutual learning module promotes collaboration among sub-networks and enhances the fusion of diverse features [13]. The experiments in Section IV-C visualize the effect of this strategy. As illustrated in Fig. 8, this module uses KL divergence to align the entropy and feature similarity of paired networks.

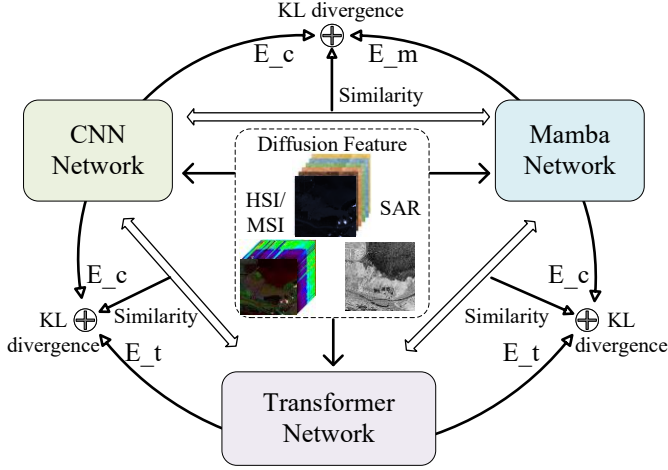


Fig. 8. Illustration of the mutual learning module.

Taking features \mathbf{f}_{cnn} and \mathbf{f}_{trans} as an example, their feature similarity is defined by cosine similarity:

$$Sim(\mathbf{f}_{cnn}, \mathbf{f}_{trans}) = \frac{\mathbf{f}_{cnn} \cdot \mathbf{f}_{trans}}{\|\mathbf{f}_{cnn}\| \|\mathbf{f}_{trans}\|}. \quad (25)$$

Each sub-network produces a classification probability \mathbf{z} , from which the categorical probability distribution is derived as:

$$\mathbf{p}^{(i)}(j) = \frac{\exp(\mathbf{z}_j^{(i)})}{\sum_{k=1}^C \exp(\mathbf{z}_k^{(i)})}, \quad (26)$$

$$H^{(i)} = - \sum_{j=1}^C \mathbf{p}^{(i)}(j) \log \mathbf{p}^{(i)}(j),$$

where $i \in B$ and $j \in C$ denote the sample and category indices, respectively, with B samples for a batch and C classes. $H^{(i)}$ represents the entropy. Thus, the classification entropies are denoted as H_{cnn} , H_{trans} , and H_{mamba} .

The similarity and entropy from (25) and (26) jointly determine the temperature in KL divergence:

$$\begin{cases} temp = (Sim(\mathbf{f}_{cnn}, \mathbf{f}_{trans}), H_{cnn} + H_{trans}), \\ T = \ln(1 + \exp(FC \cdot temp)) + 10^{-6}. \end{cases} \quad (27)$$

Integrating this adaptive temperature into the KL divergence, the mutual learning loss between the CNN and transformer networks is defined as:

$$L_{kl}^{ct} = T^2 \cdot \frac{1}{B} \sum_{i=1}^B \sum_j \mathbf{p}_{trans}^{(i)}(j) \left[\log \mathbf{p}_{trans}^{(i)}(j) - \log \mathbf{p}_{cnn}^{(i)}(j) \right]. \quad (28)$$

Similarly, the mutual learning losses L_{kl}^{cm} and L_{kl}^{tm} are computed for the other paired sub-networks. Given cross-entropy loss function L_{ce} , the final loss is expressed as:

$$\begin{cases} \mathbf{z}_{total} = FC \cdot (\mathbf{f}_{trans}, \mathbf{f}_{cnn}, \mathbf{f}_{mamba}), \\ L_{total} = L_{ce}(\mathbf{z}_{total}) + L_{kl}^{ct} + L_{kl}^{cm} + L_{kl}^{tm}. \end{cases} \quad (29)$$

IV. EXPERIMENTAL RESULTS AND DISCUSSION

Four multimodal remote sensing datasets are used to evaluate the classification performance of the proposed BDGF.

In this section, we first introduce the datasets and evaluation criteria, followed by detailed ablation experiments. Next, we visualize feature complementarity of the two modules on the LCZ HK dataset. Finally, we compare BDGF with state-of-the-art methods and discuss its transferability and computational complexity.

We compare BDGF with several state-of-the-art multimodal remote sensing classification methods, including CNN-based networks AsyFFNet [51] and CALC [23], and the pre-training method SS-MAE [36]. In addition, we include four classification methods that focus on multi-branch and multi-scale networks: Fusion-HCT [50], MACN [24], NCGLF [16], and UACL [52]. Two advanced multi-scale Mamba-based methods, HLMamba [25] and MSFMamba [20], are also evaluated.

A. Description of Datasets

1) *Berlin dataset (HSI+SAR)*: The Berlin dataset provides a comprehensive view of urban and rural regions in Berlin, Germany. It comprises HSI and SAR data, each with a spatial resolution of 30 meters and dimensions of 797×220 pixels. The HSI data, collected by the HyMap sensor (simulated for the EnMAP satellite), consist of 244 spectral bands covering 400–2500 nm. The SAR data, captured by Sentinel-1, have been processed with SNAP for orbit correction, radiometric calibration, and speckle reduction. The dataset is divided into eight distinct land-cover classes, as detailed in Table I. A pseudo-color composite of the HSI, a grayscale SAR image, and the ground-truth map are presented in Fig. 9 (a).

2) *Augsburg dataset (HSI+SAR)*: The Augsburg dataset captures a detailed rural landscape near Augsburg, Germany. It comprises a 332×485 pixel HSI and a SAR image. The HSI, acquired by the HySpex sensor, covers 180 spectral bands from 400 to 2500 nm with a 30 m ground sampling distance. The SAR image, obtained by Sentinel-1 and preprocessed by the European Space Agency using the Sentinel Application Platform, is available in both dual-polarization (VV-VH) and single-look complex (SLC) formats. The dataset is categorized into seven land-cover classes at 30 m resolution. Fig. 9 (b) visualizes the data through pseudo-color composites and a ground-truth map, while Table I summarizes the sample counts.

3) *Yellow River Estuary dataset (HSI+SAR)*: The Yellow River Estuary dataset [10] provides a detailed perspective on wetland scenes in Shandong Province, China. The dataset, comprising 960×1170 pixels with a spatial resolution of 30 meters, includes HSI and SAR data covering five land-cover classes. The HSI is acquired by the Advanced Hyperspectral Imager (AHSI) onboard the ZY1-02D satellite, covering 166 bands with spectral resolutions of 10 nm and 20 nm. Pre-processing of the HSI was performed with ENVI for radiometric and atmospheric correction. The SAR data were captured by Sentinel-1. Fig. 9 (c) displays a pseudo-color composite of the HSI, a grayscale SAR image, and the ground-truth map, with sample details provided in Table I.

4) *LCZ HK dataset (MSI+SAR)*: The Local Climate Zone Hong Kong (LCZ HK) dataset [8] offers a comprehensive view of urban and rural areas in Hong Kong, China. It includes

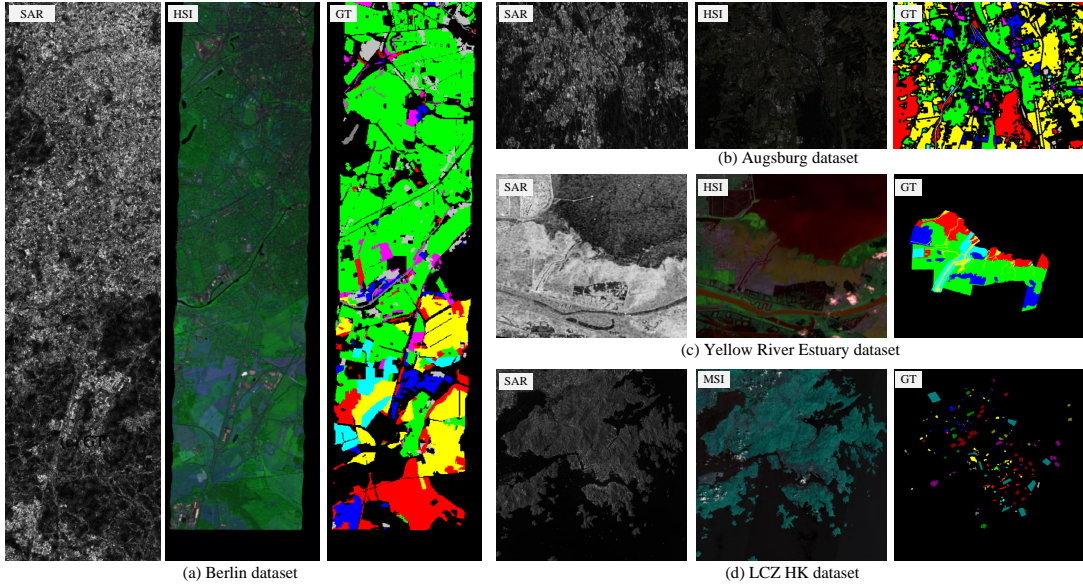


Fig. 9. Multimodal remote sensing datasets. (a) Berlin dataset. (b) Augsburg dataset. (c) Yellow River Estuary dataset. (d) LCZ HK dataset

TABLE I
LAND-COVER CLASSES AND RELATED NUMBERS OF SAMPLES IN THE FOUR CONSIDERED DATASETS

Augsburg (HSI+SAR)				Berlin (HSI+SAR)				LCZ HK (MSI+SAR)			
No.	Color	Name	Numbers	No.	Color	Name	Numbers	No.	Color	Name	Numbers
1	Red	Forest	13507	1	Red	Forest	54954	1	Red	Compact High-rise	631
2	Green	Residential Area	30329	2	Green	Residential Area	268642	2	Green	Compact Mid-rise	179
3	Blue	Industrial Area	3851	3	Blue	Industrial Area	19566	3	Blue	Compact Low-rise	326
4	Yellow	Low Plants	26857	4	Yellow	Low Plants	59282	4	Yellow	Open High-rise	673
5	Cyan	Allotment	575	5	Cyan	Soil	17426	5	Cyan	Open Mid-rise	126
6	Magenta	Commercial Area	1645	6	Magenta	Allotment	13305	6	Magenta	Open Low-rise	120
7	Grey	Water	1530	7	Grey	Commercial Area	24824	7	Grey	Large Low-rise	137
Total			78294	8	Grey	Water	6672	8	Grey	Heavy Industry	219
Yellow River Estuary (HSI+SAR)								9	Brown	Dense Trees	1616
No.	Color	Name	Numbers					10	Olive	Scattered Trees	540
1	Red	Spartina Alterniflora	39784					11	Dark Green	Bush and Scrub	691
2	Green	Suaeda Salsa	118213					12	Purple	Low Plants	985
3	Blue	Tamarix Forest	35216					13	Teal	Water	2603
4	Yellow	Tidal Creek	15673								
5	Cyan	Mudflat	24592								
Total			233478	Total			464671	Total			8846

multispectral data collected by Sentinel-2 and SAR data from Sentinel-1. The MSI consists of ten spectral bands, resampled to a 100 m resolution, with a spatial size of 529×528 pixels; the SAR image is downsampled to the same size. The dataset is divided into eight distinct land-cover classes as shown in Table I. Fig. 9 (d) presents pseudo-color composites of the MSI and SAR data alongside the ground-truth map.

In our experiments, we employ four metrics to quantitatively assess classification performance: class-specific accuracy, overall accuracy (OA), average accuracy (AA), and the kappa coefficient (Kappa). The experiments are implemented using PyTorch and executed on an NVIDIA GeForce RTX 3090 (24 GB). The denoising network follows the U-Net structure of SpectralDiff [32] but adds our masking strategy. Optimization is performed using the Adam algorithm with a learning rate of 4×10^{-4} , modulated by a MultiStepLR scheduler with a decay factor of 0.5. The patch size is 9 and the dimension of embedding features is 64. The implementation

parameter details are in the publicly available code to ensure reproducibility¹. All the comparison methods are executed under the same configurations. HSI and SAR datasets use 100 labeled samples per class, while the MSI and SAR dataset uses 50 labeled samples per class.

B. Ablation Study

To evaluate the effectiveness of the BDGF framework, we conduct a series of ablation experiments by selectively retaining key modules and sub-networks. Experiments 1–3 employ only a single network combined with diffusion features for feature extraction and classification to assess the contribution of each sub-network individually. In experiments 4–6, two networks are fused with diffusion features to evaluate their joint performance. To assess the impact of diffusion feature hierarchical guidance, experiments 7–9 are performed by removing

¹<https://github.com/HaoLiu-XDU/BDGF>

TABLE II
 OA (%) , AA (%) , AND KAPPA (%) OBTAINED IN THE ABLATION STUDY ON THE FOUR CONSIDERED DATASETS (BOLD VALUES ARE THE BEST AND UNDERLINE VALUES ARE THE SECOND)

Experiment Number	CNN	Trans	Mamba	Guide-CNN	Guide-Trans	Guide-Mamba	Mutual	Mask	Augsburg dataset			Berlin dataset			Yellow River Estuary dataset			LCZ HK dataset		
									OA	AA	Kappa	OA	AA	Kappa	OA	AA	Kappa	OA	AA	Kappa
1	✓			✓				✓	<u>93.23</u>	88.13	<u>90.41</u>	73.92	76.53	<u>64.72</u>	74.48	78.32	66.09	94.95	95.26	93.93
2		✓			✓			✓	92.02	87.00	88.79	69.60	78.53	57.50	67.57	67.35	54.79	87.46	88.81	85.00
3			✓			✓		✓	91.02	87.11	87.42	72.54	78.17	61.86	74.42	77.26	64.58	92.52	92.76	91.03
4		✓	✓		✓	✓	✓	✓	92.29	88.06	89.15	68.80	75.81	57.50	76.97	78.03	67.62	90.16	90.98	88.21
5	✓		✓	✓		✓	✓	✓	92.32	89.36	89.33	74.60	78.96	64.30	78.98	78.30	70.15	95.12	95.29	94.14
6	✓	✓		✓	✓		✓	✓	92.10	89.76	88.89	73.02	78.52	62.63	78.16	77.84	<u>71.80</u>	94.73	95.02	93.68
7	✓	✓	✓	✓	✓	✓	✓	✓	92.93	88.26	90.18	70.18	76.57	58.73	77.73	79.04	67.33	94.40	94.73	93.29
8	✓	✓	✓	✓	✓	✓	✓	✓	92.50	90.08	89.48	<u>74.78</u>	78.77	64.49	79.24	79.66	72.06	<u>95.29</u>	95.80	<u>94.35</u>
9	✓	✓	✓	✓	✓	✓	✓	✓	92.78	90.46	89.84	74.40	78.72	62.82	<u>79.27</u>	<u>80.02</u>	70.65	94.74	95.39	93.69
10	✓	✓	✓	✓	✓	✓	✓	✓	93.20	89.93	90.31	74.21	<u>78.98</u>	64.20	79.12	79.35	70.55	94.62	95.02	93.55
11	✓	✓	✓	✓	✓	✓	✓	✓	92.69	90.09	89.70	74.26	76.70	63.12	78.03	80.35	69.37	94.20	95.38	93.05
12	✓	✓	✓	✓	✓	✓	✓	✓	93.57	<u>90.12</u>	90.93	75.11	79.94	64.73	79.55	80.21	71.00	95.35	<u>95.43</u>	94.42

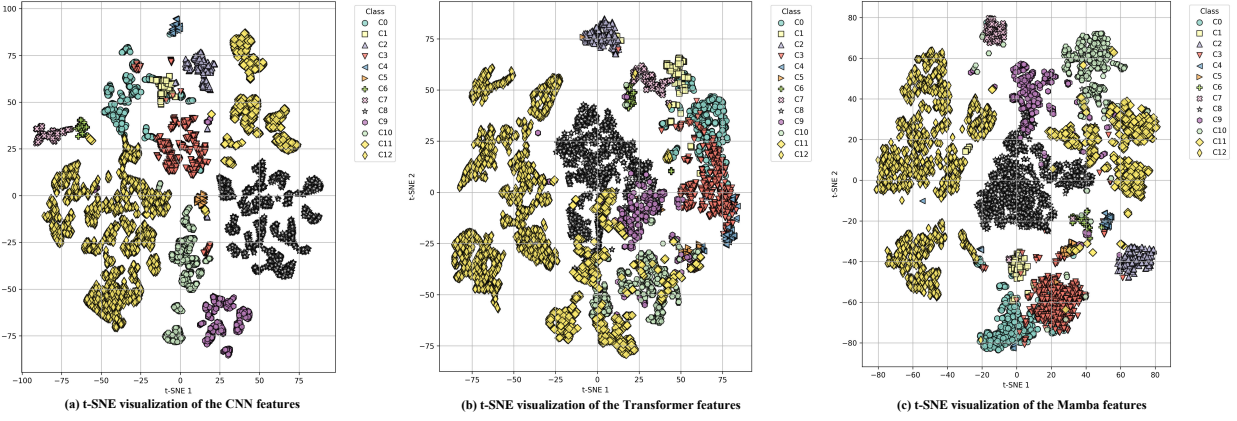


Fig. 10. 2D t-SNE embeddings of per-branch features on the LCZ HK dataset. (a)–(c) represents features from the CNN, Transformer, and Mamba branches, respectively.

the respective guidance branches. Finally, experiments 10 and 11 remove the adaptive modality mask strategy and the mutual learning module, respectively, to demonstrate their individual contributions. In Table II, “CNN,” “Trans,” and “Mamba” denote networks based on CNN, transformer, and Mamba architectures, while “Guide-CNN,” “Guide-Trans,” and “Guide-Mamba” indicate the corresponding diffusion feature guidance modules. “Mutual” and “Mask” represent the mutual learning module and the adaptive modality mask strategy, respectively.

The experimental results are presented in Table II. In general, the following conclusions can be drawn:

- 1) Experiments 1–3 indicate that the CNN network alone yields superior classification performance than other networks. Similarly, in experiments 4–6, performance noticeably declines when the CNN network is removed, underscoring the importance of integrating local and global features to extract diverse information from multimodal models.
- 2) Experiments 2, 3, 5, and 6 demonstrate that a self-attention-based transformer alone is not effective, suggesting that relying solely on global feature extraction is limited. In contrast, the Mamba network outperforms the

transformer, highlighting its advantage in modeling long sequences in spectral images.

- 3) Comparisons between experiments 7–9 and the corresponding experiments 4–6 without diffusion feature guidance reveal that models incorporating additional sub-networks perform better, which confirms the significance of diverse features.
- 4) Finally, experiments 10 and 11 show that removing the mutual learning module and the adaptive modality mask strategy leads to a decline in performance, thereby verifying the effectiveness of these modules. Experiment 12 further demonstrates that the proposed model achieves excellent results.

C. Feature Complementarity Visualization

To verify that our multi-branch architecture learns complementary representations, we visualize the per-branch features immediately before the final fusion layer. Fig. 10 shows features extracted from the LCZ HK dataset (13 classes, 50 samples per class) projected onto two dimensions via t-distributed stochastic neighbor embedding (t-SNE). The t-SNE projection is generated from the first 50 principal components

TABLE III
CLASSIFICATION ACCURACIES (%) ON THE AUGSBURG DATASET WITH 100 TRAINING SAMPLES FOR EACH CLASS (BOLD VALUES ARE THE BEST AND UNDERLINE VALUES ARE THE SECOND)

Class	AsyFFNet	CALC	Fusion-HCT	MACN	NCGLF	UACL	SS-MAE	HLMamba	MSFMamba	BDGF
1	94.32	95.67	96.32	96.84	92.32	93.51	<u>97.52</u>	97.51	97.78	97.03±0.80
2	85.80	<u>89.96</u>	85.89	86.89	89.55	89.94	89.21	89.07	89.61	91.74±1.71
3	<u>85.28</u>	51.37	78.81	73.21	70.00	64.09	75.58	35.54	62.06	87.28±1.04
4	91.51	90.04	94.32	94.48	94.38	95.79	95.56	96.25	94.73	<u>96.13±0.82</u>
5	96.84	55.79	96.84	96.42	93.96	95.30	98.11	93.68	96.63	<u>97.20±0.86</u>
6	69.64	96.50	62.72	61.55	73.40	<u>90.03</u>	71.52	89.32	66.60	84.06±3.81
7	82.66	76.85	74.20	79.30	80.03	<u>77.45</u>	80.98	<u>81.26</u>	77.00	77.41±1.64
OA	88.91	88.79	89.65	89.98	90.23	91.09	<u>91.73</u>	90.31	90.81	93.57±0.51
AA	86.58	79.46	84.15	84.10	84.81	86.59	<u>86.93</u>	83.23	83.49	90.12±0.75
Kappa	84.62	84.29	85.60	86.01	86.37	87.53	<u>88.40</u>	86.41	87.13	90.93±0.70

TABLE IV
CLASSIFICATION ACCURACIES (%) ON THE YELLOW RIVER ESTUARY DATASET WITH 100 TRAINING SAMPLES FOR EACH CLASS (BOLD VALUES ARE THE BEST AND UNDERLINE VALUES ARE THE SECOND)

Class	AsyFFNet	CALC	Fusion-HCT	MACN	NCGLF	UACL	SS-MAE	HLMamba	MSFMamba	BDGF
1	91.54	86.14	91.55	92.34	90.63	<u>91.92</u>	90.48	86.20	88.74	88.23±0.93
2	69.91	<u>73.48</u>	67.55	65.78	71.03	<u>64.07</u>	69.11	71.37	72.28	76.72±2.50
3	75.24	64.48	83.97	86.25	88.98	71.67	80.72	88.84	<u>88.88</u>	81.00±3.71
4	<u>79.78</u>	71.87	77.35	79.65	76.29	77.00	78.80	82.02	77.55	75.57±1.59
5	83.12	89.36	76.45	74.01	76.19	80.85	<u>84.98</u>	78.49	80.28	79.54±4.00
OA	76.45	75.84	75.70	75.18	77.97	72.08	76.81	77.99	<u>78.78</u>	79.55±1.29
AA	79.92	77.07	79.37	79.60	80.62	76.90	80.82	<u>81.38</u>	81.55	80.21±1.25
Kappa	67.50	66.17	66.70	66.08	69.60	62.16	68.13	69.63	<u>70.63</u>	71.00±1.65

TABLE V
CLASSIFICATION ACCURACIES (%) ON THE BERLIN DATASET WITH 100 TRAINING SAMPLES FOR EACH CLASS (BOLD VALUES ARE THE BEST AND UNDERLINE VALUES ARE THE SECOND)

Class	AsyFFNet	CALC	Fusion-HCT	MACN	NCGLF	UACL	SS-MAE	HLMamba	MSFMamba	BDGF
1	81.29	81.65	79.67	84.96	<u>89.86</u>	88.93	88.14	89.66	89.87	82.34±5.48
2	69.62	<u>71.16</u>	68.04	65.84	67.63	72.06	67.46	66.93	68.73	70.87±3.81
3	62.05	64.68	64.73	64.94	67.65	66.99	<u>68.08</u>	67.13	67.52	76.81±3.95
4	82.04	84.25	89.51	86.72	85.69	82.55	<u>87.47</u>	80.80	84.04	85.97±3.13
5	93.06	94.01	96.09	94.37	95.27	88.96	93.04	92.81	96.66	<u>96.12±2.35</u>
6	74.09	84.97	80.33	<u>85.02</u>	86.69	53.00	83.88	80.83	83.18	74.95±7.08
7	60.12	51.31	57.20	52.93	62.16	21.66	<u>60.98</u>	54.02	60.04	57.95±4.17
8	91.19	92.82	92.44	80.14	<u>94.79</u>	95.05	93.39	92.79	85.48	94.49±2.02
OA	73.07	74.29	73.18	71.85	74.24	72.90	73.93	72.44	<u>74.36</u>	75.11±1.49
AA	76.68	78.11	78.50	76.86	81.22	61.26	80.31	78.12	79.44	79.94±1.90
Kappa	61.83	63.72	62.64	61.16	64.55	71.15	63.76	61.84	64.29	<u>64.73±1.58</u>

of the data, using a perplexity of 30 and 1000 iterations to ensure reproducible results.

The three branch features capture complementary structure. For example, CNN features show intermixing of classes C0 and C2 that are cleanly separated by Transformer features, while Mamba features produce distinct islands for classes such as C5 and C8 that appear split or overlapped in the other embeddings. Notably, C11 is fragmented into multiple local modes in the CNN plot, whereas it becomes consolidated in the Transformer plot, and occupies largely non-overlapping regions in the Mamba plot. Similar complementary behaviours are observed for C3 and C7, suggesting that feature fusion may improve class separability.

D. Classification Results

To illustrate the effectiveness of the proposed BDGF, we conducted a comparative analysis with ten state-of-the-art multimodal classification models. AsyFFNet employs an asymmetric neural network with weight-sharing residual blocks for multimodal feature extraction and introduces a channel

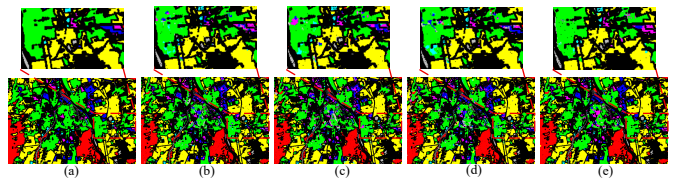


Fig. 11. Classification maps and OA% obtained on the Augsburg dataset using several methods. (a) Ground-truth map. (b) SS-MAE (91.73%). (c) HLMamba (90.31%). (d) MSFMamba (90.81%). (e) BDGF (93.57%).

exchange mechanism with sparse constraints for feature fusion. CALC builds a multi-level feature fusion module and a spatial attention-guided discriminator based on CNNs and generative adversarial networks. SS-MAE adopts a similar network architecture but incorporates pre-training and masked self-supervised strategies.

Furthermore, we selected four methods that focus on multi-branch network structures. Fusion-HCT and MACN integrate CNNs and transformers to capture both local and global features, introducing innovative attention mechanisms for multi-

TABLE VI
CLASSIFICATION ACCURACIES (%) ON THE LCZ HK DATASET WITH 50 TRAINING SAMPLES FOR EACH CLASS (BOLD VALUES ARE THE BEST AND UNDERLINE VALUES ARE THE SECOND)

Class	AsyFFNet	CALC	Fusion-HCT	MACN	NCGLF	UACL	SS-MAE	HLMamba	MSFMamba	BDGF
1	64.37	77.62	72.46	53.53	76.40	68.67	78.14	74.87	83.30	<u>80.77</u> ±3.20
2	95.35	66.67	80.62	86.82	90.67	34.11	89.15	<u>96.12</u>	73.64	97.05 ±2.05
3	89.13	97.10	<u>97.46</u>	97.46	93.83	97.10	92.03	93.48	96.38	99.02 ±0.67
4	80.90	<u>93.74</u>	81.70	91.97	87.31	78.97	93.94	76.08	86.84	90.16±1.97
5	97.37	94.74	<u>98.68</u>	97.37	<u>99.68</u>	98.68	94.74	89.47	93.42	99.87 ±0.39
6	100.00	100.00	92.86	98.57	<u>99.33</u>	87.14	<u>98.57</u>	98.57	88.57	97.14±0.14
7	95.40	93.10	94.25	94.25	95.84	95.40	100.00	83.06	96.55	<u>99.66</u> ±0.53
8	93.49	96.45	89.94	98.22	96.67	100.00	97.63	94.08	92.31	<u>98.58</u> ±0.71
9	94.70	98.08	94.76	94.76	97.17	96.87	95.59	93.04	94.89	<u>97.48</u> ±2.04
10	82.45	87.76	84.90	84.90	87.02	84.90	<u>90.82</u>	80.41	61.02	91.94 ±1.55
11	71.76	91.11	92.82	82.37	<u>94.63</u>	80.97	90.02	87.99	86.90	96.93 ±0.80
12	81.28	77.22	85.78	74.65	85.01	<u>89.73</u>	84.17	68.66	87.38	93.52 ±1.24
13	98.12	97.61	96.91	99.69	<u>97.07</u>	<u>99.61</u>	99.10	98.55	97.57	98.53±0.69
OA	88.38	91.98	90.87	89.40	92.51	90.59	<u>93.16</u>	88.26	90.40	95.35 ±0.58
AA	88.03	90.09	89.47	88.81	92.36	88.73	<u>92.59</u>	87.41	87.60	95.43 ±0.37
Kappa	86.09	90.38	89.09	87.29	91.16	85.55	<u>91.79</u>	85.95	88.49	94.42 ±0.69

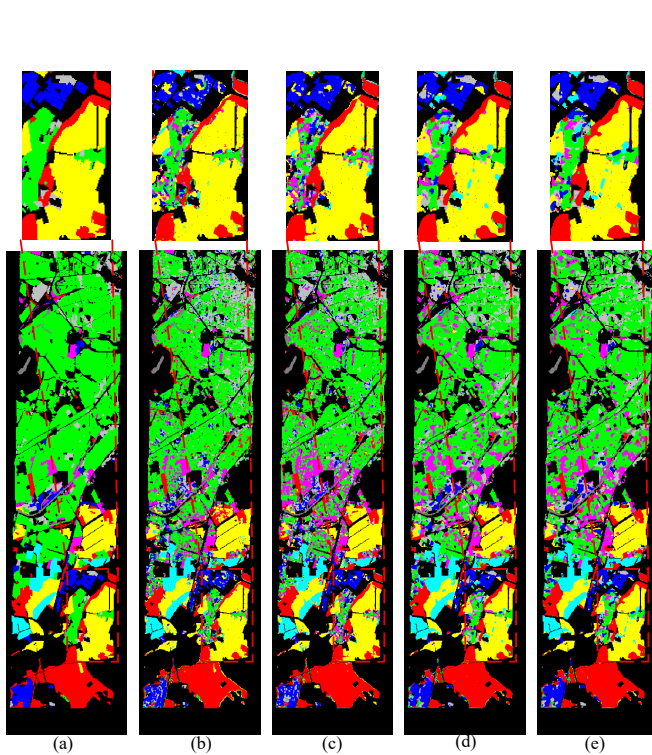


Fig. 12. Classification maps and OA% obtained on the Berlin dataset using several methods. (a) Ground-truth map. (b) SS-MAE (73.93%). (c) HLMamba (72.44%). (d) MSFMamba (74.36%). (e) BDGF (75.11%).

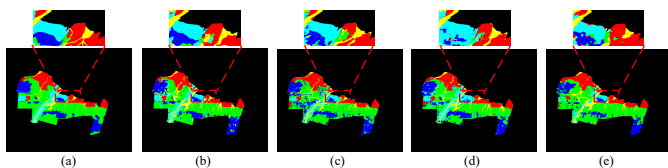


Fig. 13. Classification maps and OA% obtained on the Yellow River Estuary dataset using several methods. (a) Ground-truth map. (b) SS-MAE (76.81%). (c) HLMamba (77.99%). (d) MSFMamba (78.78%). (e) BDGF (79.55%).

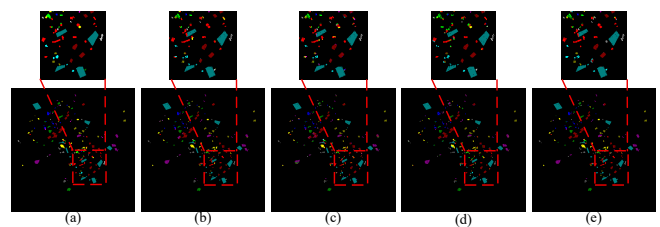


Fig. 14. Classification maps and OA% obtained on the LCZ HK dataset using several methods. (a) Ground-truth map. (b) SS-MAE (93.16%). (c) HLMamba (88.26%) (d) MSFMamba (90.40%). (e) BDGF (95.35%).

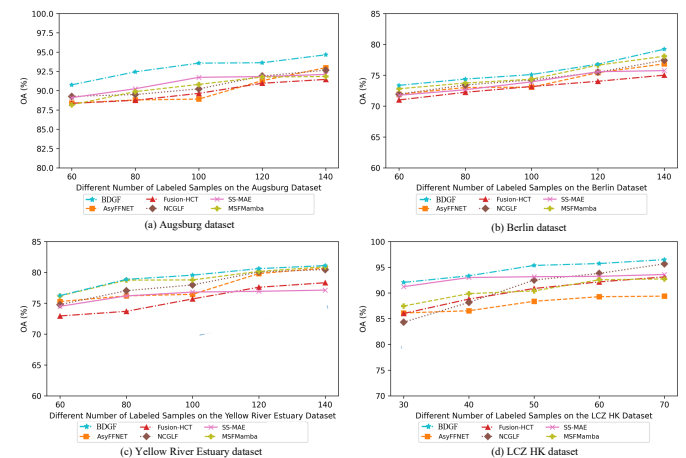


Fig. 15. OA% versus the number of labeled samples on the four LCZ considered datasets. (a) Augsburg dataset. (b) Berlin dataset. (c) Yellow River Estuary dataset. (d) LCZ HK dataset.

modal feature fusion. NCGLF enhances CNN and transformer structures with structural information learning and invertible neural networks. UACL proposes a contrastive learning strategy to access reliable multimodal samples. In addition, two recent multimodal learning methods based on the multi-scale Mamba structure are included for comparison. HLMamba constructs a multimodal Mamba fusion module and introduces a gradient joint algorithm to enhance modality information, while MSFMamba employs spatial, spectral, and fused Mamba branches with a large effective receptive field to achieve multi-scale feature fusion.

TABLE VII
NUMBER OF PARAMETERS (M, MILLION) AND GFLOPS OF DIFFERENT CONSIDERED METHODS

		AsyFFNET	CALC	Fusion-HCT	MACN	NCGLF	UACL	HLMamba	MSFMamba	SS-MAE (P)	SS-MAE (T)	BDGF (P)	BDGF (T)
Augsburg	Params. (M)	1.08	0.94	0.43	0.17	0.44	0.19	0.23	0.82	7.72	4.51	4.30	16.38
	GFLOPs	17.76	7.23	0.59	0.70	8.72	2.38	22.68	25.17	74.21	51.34	996.43	99.33
Yellow River Estuary	Params. (M)	1.08	0.92	0.43	0.17	0.44	0.18	0.20	0.78	7.70	4.50	4.30	9.56
	GFLOPs	17.72	6.80	0.59	0.70	8.72	2.24	14.67	25.15	69.54	48.13	498.22	64.28
Berlin	Params. (M)	1.06	0.99	0.43	0.17	0.44	0.21	0.19	2.46	7.80	4.54	4.30	16.38
	GFLOPs	17.35	9.04	0.59	0.70	8.72	2.99	12.77	61.91	94.69	65.02	996.43	99.33
LCZ HK	Params. (M)	1.06	0.79	0.43	0.07	0.34	0.13	0.18	0.21	7.56	4.44	4.30	6.15
	GFLOPs	17.32	2.47	0.59	0.37	7.07	0.80	11.58	3.83	23.29	17.15	124.55	46.12

The performance of these classification methods is summarized in Tables III–VI. For a visual comparison, the respective segmentation maps of several methods are presented in Figs. 11-14. To further verify the effectiveness of the model on different training samples, we conducted experiments with 60, 80, 120, and 140 labeled samples per class for HSI and SAR classification, and 30, 40, 60, and 70 labeled samples per class for MSI and SAR classification. The performance of each method under these settings is illustrated in Fig. 15. Based on these outcomes, the following conclusions can be drawn:

- 1) Methods that integrate multi-scale and multi-branch architectures for multimodal data fusion exhibit superior classification performance. Among these, NCGLF outperforms the two CNN-based methods due to its effective integration of global and local information.
- 2) SS-MAE, which learns multimodal features through a reconstructed pre-training paradigm, achieved suboptimal classification results on the Augsburg and LCZ HK datasets. Similarly, MSFMamba, which employs a multi-scale network with Mamba as its core, obtained suboptimal results on the other two datasets.
- 3) Leveraging guidance from robust diffusion features, the proposed BDGF improves collaborative learning of multimodal features across different branches, as evidenced by its highest OA index along with excellent AA and kappa values. On the four datasets, BDGF consistently outperforms previous state-of-the-art models by 1.84%, 0.77%, 0.75%, and 2.19% in OA index, respectively. As one can see from the figures and the tables, in the Augsburg and Berlin datasets, the proposed BDGF achieves high classification results in the “residential area” and “industrial area” categories. Among the 13 categories in the LCZ HK dataset, the BDGF has the highest semantic classification accuracy on 6 classes.
- 4) Different methods exhibited differing levels of sensitivity to the number of labeled samples. However, across all configurations, the proposed BDGF framework consistently achieved the highest classification accuracy.

E. Analysis of the Computational Complexity

In this section, we evaluate the computational complexity of all models in terms of GFLOPs and number of parameters (millions). Table VII presents these metrics for the four datasets considered. Note that SS-MAE and BDGF employ

TABLE VIII
CLASSIFICATION ACCURACIES (%) IN THE CROSS-MODEL FEATURE TRANSFER EXPERIMENTS ON THE FOUR CONSIDERED DATASETS

Dataset	Attention Classified Module					
	Masking Diff			Concatenate Diff		
	OA	AA	Kappa	OA	AA	Kappa
Augsburg	70.72	56.41	46.34	67.15	64.06	55.64
Berlin	63.73	65.05	54.56	42.24	22.44	18.35
Yellow River Estuary	68.26	64.78	59.49	63.04	48.23	38.74
LCZ HK	91.75	93.12	90.12	91.24	91.40	89.71

Dataset	Multi-Branch Network					
	Masking Diff			Concatenate Diff		
	OA	AA	Kappa	OA	AA	Kappa
Augsburg	93.57	90.12	90.93	92.62	89.90	89.59
Berlin	75.11	79.94	64.73	74.30	77.38	63.50
Yellow River Estuary	79.55	80.21	71.00	77.85	80.16	69.02
LCZ HK	95.35	95.43	94.42	95.06	95.07	94.07

a pre-training paradigm, and (P) and (T) denote pre-training and training phases, respectively. Under unsupervised learning, larger models generally generalize better. Pre-training methods incur higher computational costs than other approaches, and adopting a dual-branch structure for the pre-training auto-encoder and diffusion model further increases complexity. SS-MAE and BDGF mitigate this issue by merging multimodal images along the channel dimension. Their superior classification results across the four datasets confirm the effectiveness of pre-training. For the proposed BDGF, the parameter count arises from integrating multi-branch sub-networks, while the FLOPs reflect the diffusion model’s pre-training. Although BDGF exhibits higher computational complexity, it remains within acceptable limits and achieves the best classification performance.

F. Analysis of the Transferability

Different from the fine-tuning training paradigm such as SS-MAE, the proposed BDGF framework employs an unsupervised diffusion process to learn the joint data distribution of multimodal images and directly leverages these

learned features for downstream classification. To evaluate both the transferability of our adaptive masking strategy and the modularity of our multi-branch network, we perform cross-model feature-transfer experiments with SpectralDiff [32], which shares a similar training paradigm. Specifically, we first adapt SpectralDiff to multimodal inputs using early fusion via channel-wise concatenation [8], [16], [44]. From the pre-trained diffusion backbones of both methods, we extract features and graft them into the other model's classification head. In Table VIII, the pre-trained diffusion model and sub-network of SpectralDiff are denoted as "Concatenate Diff" and "Attention Classified Module", respectively, while the corresponding annotations of our method are "Masking Diff" and "Multi-Branch Network".

As one can see from the Table VIII, with the same classifier backbone, the adaptive masking strategy consistently enhances performance. Moreover, using identical pre-trained diffusion features, the multi-branch network outperforms SpectralDiff's attention-based classification module across all datasets. Notably, on the Augsburg dataset, the attention classification module suffers a substantial accuracy drop, which shows the superior robustness of our multi-branch fusion in capturing diverse features.

V. CONCLUSION

In this paper, we have proposed the balanced diffusion-guided fusion (BDGF) framework for multimodal remote sensing image classification. BDGF leverages robust diffusion features to guide a multi-branch network that integrates CNN, transformer, and Mamba networks. An adaptive modality masking strategy is introduced to mitigate modality imbalance during pre-training, ensuring a balanced representation between spectral and SAR images. In addition, the diffusion features are hierarchically fused through feature fusion, group attention mechanism, and cross-attention mechanism. Finally, a mutual learning strategy coordinates the predictions of each sub-network to improve the overall performance.

Extensive experiments on four multimodal remote sensing datasets validate the effectiveness of BDGF. Ablation studies confirm the contribution of each feature guidance module and strategy, and comparative evaluations under varying numbers of labeled samples demonstrate that BDGF sharply outperforms state-of-the-art methods in terms of classification accuracy. In addition, in cross-model feature-transfer experiments with SpectralDiff, the two-stage BDGF exhibits robust transferability. Furthermore, visualizations of diversity features on the LCZ HK dataset demonstrate the complementary nature of the proposed method's features. Computational complexity analysis shows that pre-training models (autoencoders, diffusion models) are costly, underscoring the efficiency gains of a single-branch pre-training strategy.

While BDGF significantly improves multimodal feature fusion and classification accuracy, there remains room for further enhancement. Future work will focus on more efficient pre-training paradigms and multi-task learning methods to enhance inter-network collaboration. In addition, the framework will be further extended to other remote sensing applications, such as scene classification and change detection.

REFERENCES

- [1] G. Vivone, L.-J. Deng, S. Deng, D. Hong, M. Jiang, C. Li, W. Li, H. Shen, X. Wu, J.-L. Xiao, J. Yao, M. Zhang, J. Chanussot, S. Garcia, and A. Plaza, "Deep learning in remote sensing image fusion: Methods, protocols, data, and future perspectives," *IEEE Geosci. Remote Sens. Mag.*, vol. 13, no. 1, pp. 269–310, Mar. 2025.
- [2] C. He, B. Gao, Q. Huang, Q. Ma, and Y. Dou, "Environmental degradation in the urban areas of china: Evidence from multi-source remote sensing data," *Remote Sens. Environ.*, vol. 193, pp. 65–75, Mar. 2017.
- [3] Z. Han, Y. Gao, X. Jiang, J. Wang, and W. Li, "Multisource remote sensing classification for coastal wetland using feature intersecting learning," *IEEE Geosci. Remote Sens. Lett.*, vol. 19, pp. 1–5, Mar. 2022.
- [4] X. Ma, C. Li, X. Tong, and S. Liu, "A new fusion approach for extracting urban built-up areas from multisource remotely sensed data," *Remote Sens.*, vol. 11, no. 21, p. 2516, Oct. 2019.
- [5] J. Zhang, "Multi-source remote sensing data fusion: status and trends," *Int. J. Image Data fusion*, vol. 1, no. 1, pp. 5–24, Feb. 2010.
- [6] M. Khodadadzadeh, J. Li, S. Prasad, and A. Plaza, "Fusion of hyperspectral and lidar remote sensing data using multiple feature learning," *IEEE J. Sel. Topics Appl. Earth Observ. Remote Sens.*, vol. 8, no. 6, pp. 2971–2983, Jun. 2015.
- [7] Y. Gao, W. Li, J. Wang, M. Zhang, and R. Tao, "Relationship learning from multisource images via spatial-spectral perception network," *IEEE Trans. Image Process.*, vol. 33, pp. 3271–3284, May 2024.
- [8] D. Hong, L. Gao, N. Yokoya, J. Yao, J. Chanussot, Q. Du, and B. Zhang, "More diverse means better: Multimodal deep learning meets remote-sensing imagery classification," *IEEE Trans. Geosci. and Remote Sens.*, vol. 59, no. 5, pp. 4340–4354, Aug. 2021.
- [9] X. Wu, D. Hong, and J. Chanussot, "Convolutional neural networks for multimodal remote sensing data classification," *IEEE Trans. Geosci. Remote Sens.*, vol. 60, pp. 1–10, Feb. 2022.
- [10] Y. Gao, X. Song, W. Li, J. Wang, J. He, X. Jiang, and Y. Feng, "Fusion classification of hsi and msi using a spatial-spectral vision transformer for wetland biodiversity estimation," *Remote Sens.*, vol. 14, no. 4, p. 850, Feb. 2022.
- [11] Z. Xue, X. Tan, X. Yu, B. Liu, A. Yu, and P. Zhang, "Deep hierarchical vision transformer for hyperspectral and lidar data classification," *IEEE Trans. Image Process.*, vol. 31, pp. 3095–3110, Apr. 2022.
- [12] S. K. Roy, A. Deria, D. Hong, B. Rasti, A. Plaza, and J. Chanussot, "Multimodal fusion transformer for remote sensing image classification," *IEEE Trans. Geosci. Remote Sens.*, vol. 61, pp. 1–20, Jun. 2023.
- [13] J. Wang and X. Tan, "Mutually beneficial transformer for multimodal data fusion," *IEEE Trans. Circuits Syst. Video Technol.*, vol. 33, no. 12, pp. 7466–7479, May 2023.
- [14] Y. Wei, H. Li, J. Wang, Y. Zheng, J. Pan, and Q. Du, "Multimodal quaternion representation network for multisource remote sensing data classification," *IEEE Trans. Neural Netw. Learn. Syst.*, pp. 1–15, Sep. 2025.
- [15] K. Ni, D. Wang, Z. Zheng, and P. Wang, "Mhst: Multiscale head selection transformer for hyperspectral and lidar classification," *IEEE J. Sel. Topics Appl. Earth Observ. Remote Sens.*, vol. 17, pp. 5470–5483, Feb. 2024.
- [16] B. Tu, Q. Ren, J. Li, Z. Cao, Y. Chen, and A. Plaza, "Ncglf2: Network combining global and local features for fusion of multisource remote sensing data," *Inf. Fusion*, vol. 104, p. 102192, Apr. 2024.
- [17] A. Gu and T. Dao, "Mamba: Linear-time sequence modeling with selective state spaces," *arXiv preprint arXiv:2312.00752*, 2023.
- [18] W.-L. Du, Y. Gu, J. Zhao, H. Zhu, R. Yao, and Y. Zhou, "A mamba-diffusion framework for multimodal remote sensing image semantic segmentation," *IEEE Geosci. and Remote Sens. Lett.*, vol. 21, pp. 1–5, Oct. 2024.
- [19] G. Zhang, Z. Zhang, J. Deng, L. Bian, and C. Yang, "S2crossmamba: Spatial-spectral cross-mamba for multimodal remote sensing image classification," *IEEE Geosci. Remote Sens. Lett.*, vol. 21, pp. 1–5, Oct. 2024.
- [20] F. Gao, X. Jin, X. Zhou, J. Dong, and Q. Du, "Msfmamba: Multiscale feature fusion state space model for multisource remote sensing image classification," *IEEE Trans. Geosci. Remote Sens.*, vol. 63, pp. 1–16, Jan. 2025.
- [21] R. Du, X. Tang, J. Ma, X. Zhang, and L. Jiao, "Mlmamba: A mamba-based efficient network for multi-label remote sensing scene classification," *IEEE Trans. Circuits Syst. Video Technol.*, pp. 1–1, Jan. 2025.
- [22] S.-B. Chen, Q.-S. Wei, W.-Z. Wang, J. Tang, B. Luo, and Z.-Y. Wang, "Remote sensing scene classification via multi-branch local attention network," *IEEE Trans. Image Process.*, vol. 31, pp. 99–109, Nov. 2021.

- [23] T. Lu, K. Ding, W. Fu, S. Li, and A. Guo, "Coupled adversarial learning for fusion classification of hyperspectral and lidar data," *Inf. Fusion*, vol. 93, pp. 118–131, May 2023.
- [24] K. Li, D. Wang, X. Wang, G. Liu, Z. Wu, and Q. Wang, "Mixing self-attention and convolution: A unified framework for multi-source remote sensing data classification," *IEEE Trans. Geosci. Remote Sens.*, vol. 61, pp. 1–16, Sep. 2023.
- [25] D. Liao, Q. Wang, T. Lai, and H. Huang, "Joint classification of hyperspectral and lidar data based on mamba," *IEEE Trans. Geosci. Remote Sens.*, vol. 62, pp. 1–15, Oct. 2024.
- [26] Y. Gao, M. Zhang, W. Li, and R. Tao, "Distribution-independent domain generalization for multisource remote sensing classification," *IEEE Trans. Neural Netw. Learn. Syst.*, vol. 36, no. 7, Jul. 2025.
- [27] M. Ahmad, S. Distifano, A. M. Khan, M. Mazzara, C. Li, H. Li, J. Aryal, Y. Ding, G. Vivone, and D. Hong, "A comprehensive survey for hyperspectral image classification: The evolution from conventional to transformers and mamba models," *arXiv preprint arXiv:2404.14955*, 2024.
- [28] Y. Liu, J. Yue, S. Xia, P. Ghamisi, W. Xie, and L. Fang, "Diffusion models meet remote sensing: Principles, methods, and perspectives," *IEEE Trans. Geosci. Remote Sens.*, vol. 62, pp. 1–22, Sep. 2024.
- [29] J. Ho, A. Jain, and P. Abbeel, "Denoising diffusion probabilistic models," in *Proc. Adv. Neural. Inf. Process. Syst.*, vol. 33, Dec. 2020, pp. 6840–6851.
- [30] S. Mukhopadhyay, M. Gwilliam, V. Agarwal, N. Padmanabhan, A. Swaminathan, S. Hegde, T. Zhou, and A. Shrivastava, "Diffusion models beat gans on image classification," *arXiv preprint arXiv:2307.08702*, 2023.
- [31] J. Chen, S. Liu, Z. Zhang, and H. Wang, "Diffusion subspace clustering for hyperspectral images," *IEEE J. Sel. Topics Appl. Earth Observ. Remote Sens.*, vol. 16, pp. 6517–6530, Jul. 2023.
- [32] N. Chen, J. Yue, L. Fang, and S. Xia, "Spectraldiff: A generative framework for hyperspectral image classification with diffusion models," *IEEE Trans. Geosci. Remote Sens.*, vol. 61, pp. 1–16, Aug. 2023.
- [33] N. Sigger, Q.-T. Vien, S. V. Nguyen, G. Tozzi, and T. T. Nguyen, "Unveiling the potential of diffusion model-based framework with transformer for hyperspectral image classification," *Sci. Rep.*, vol. 14, no. 1, p. 8438, Apr. 2024.
- [34] J. Zhou, J. Sheng, P. Ye, J. Fan, T. He, B. Wang, and T. Chen, "Exploring multi-timestep multi-stage diffusion features for hyperspectral image classification," *IEEE Trans. Geosci. Remote Sens.*, vol. 62, pp. 1–16, May 2024.
- [35] G. Zhang, L. Zhang, Z. Zhang, J. Deng, L. Bian, and C. Yang, "Dect: Diffusion-enhanced cnn-transformer for multisource remote sensing data classification," *IEEE J. Sel. Topics Appl. Earth Observ. Remote Sens.*, vol. 17, pp. 19288–19301, Oct. 2024.
- [36] J. Lin, F. Gao, X. Shi, J. Dong, and Q. Du, "Ss-mae: Spatial-spectral masked autoencoder for multisource remote sensing image classification," *IEEE Trans. Geosci. Remote Sens.*, vol. 61, pp. 1–14, Nov. 2023.
- [37] N. Neverova, C. Wolf, G. Taylor, and F. Nebout, "Moddrop: Adaptive multi-modal gesture recognition," *IEEE Trans. Pattern Anal. Mach. Intell.*, vol. 38, no. 8, pp. 1692–1706, Aug. 2016.
- [38] W. Wang, D. Tran, and M. Feiszli, "What makes training multi-modal classification networks hard?" in *Proc. IEEE Conf. Comput. Vis. Pattern Recognit. (CVPR)*, Jun. 2020.
- [39] Y. Wei, D. Hu, H. Du, and J.-R. Wen, "On-the-fly modulation for balanced multimodal learning," *IEEE Trans. Pattern Anal. Mach. Intell.*, vol. 47, no. 1, pp. 469–485, Jan. 2025.
- [40] J. Jia, G. Lee, Z. Wang, L. Zhi, and Y. He, "Siamese meets diffusion network: Smdnet for enhanced change detection in high-resolution rs imagery," *IEEE J. Sel. Topics Appl. Earth Observ. Remote Sens.*, 2024.
- [41] X. Zhang, S. Tian, G. Wang, H. Zhou, and L. Jiao, "Diffucd: Unsupervised hyperspectral image change detection with semantic correlation diffusion model," *arXiv preprint arXiv:2305.12410*, 2023.
- [42] Y. Liu, Z. Sun, B. Yu, Y. Zhao, B. Du, Y. Xu, and J. Cheng, "Mifnet: Learning modality-invariant features for generalizable multimodal image matching," *IEEE Trans. Image Process.*, vol. 34, pp. 3593–3608, Jan. 2025.
- [43] S. Chen, P. Sun, Y. Song, and P. Luo, "Diffusiondet: Diffusion model for object detection," in *Proc. Int. Conf. Comput. Vis. (ICCV)*, 2023, pp. 19830–19843.
- [44] J. Li, D. Hong, L. Gao, J. Yao, K. Zheng, B. Zhang, and J. Chanussot, "Deep learning in multimodal remote sensing data fusion: A comprehensive review," *Int. J. Appl. Earth Observ. Geoinf.*, vol. 112, p. 102926, Aug. 2022.
- [45] J.-S. Lee, "Speckle analysis and smoothing of synthetic aperture radar images," *Comput. Graph. Image Process.*, vol. 17, no. 1, pp. 24–32, 1981.
- [46] J. Wang, M. Zhang, W. Li, and R. Tao, "A multistage information complementary fusion network based on flexible-mixup for hsi-x image classification," *IEEE Trans. Neural Netw. Learn. Syst.*, vol. 35, no. 12, pp. 17189–17201, Dec. 2024.
- [47] H. Liu, M. Zhang, Z. Di, M. Gong, T. Gao, and A. K. Qin, "A hybrid multi-task learning network for hyperspectral image classification with few labels," *IEEE Trans. Geosci. Remote Sens.*, vol. 62, pp. 1–16, Jan. 2024.
- [48] W. Yu and X. Wang, "Mambaout: Do we really need mamba for vision?" *arXiv preprint arXiv:2405.07992*, 2024.
- [49] J. Wang, W. Li, Y. Gao, M. Zhang, R. Tao, and Q. Du, "Hyperspectral and sar image classification via multiscale interactive fusion network," *IEEE Trans. Neural Netw. Learn. Syst.*, vol. 34, no. 12, pp. 10823–10837, Dec. 2023.
- [50] G. Zhao, Q. Ye, L. Sun, Z. Wu, C. Pan, and B. Jeon, "Joint classification of hyperspectral and lidar data using a hierarchical cnn and transformer," *IEEE Trans. Geosci. Remote Sens.*, vol. 61, pp. 1–16, Jan. 2023.
- [51] W. Li, Y. Gao, M. Zhang, R. Tao, and Q. Du, "Asymmetric feature fusion network for hyperspectral and sar image classification," *IEEE Trans. Neural Netw. Learn. Syst.*, vol. 34, no. 10, pp. 8057–8070, Oct. 2023.
- [52] K. Ding, T. Lu, and S. Li, "Uncertainty-aware contrastive learning for semi-supervised classification of multimodal remote sensing images," *IEEE Trans. Geosci. Remote Sens.*, vol. 62, pp. 1–13, May 2024.